Draft version April 13, 2024
Typeset using LaTeX **twocolumn** style in AASTeX631

A Yebes W band Line Survey towards an Unshocked Molecular Cloud of Supernova Remnant 3C391: Evidence of Cosmic-Ray-Induced Chemistry

Tian-yu Tu (涂天宇) [1], Prathap Rayalacheruvu [2,3], Liton Majumdar [2,3], Yang Chen (陈阳) [1,4], Ping Zhou (周平) [1,4] and Miguel Santander-García [5]

[1] *School of Astronomy & Space Science, Nanjing University, 163 Xianlin Avenue, Nanjing 210023, China*
[2] *School of Earth and Planetary Sciences, National Institute of Science Education and Research, Jatni 752050, Odisha, India*
[3] *Homi Bhabha National Institute, Training School Complex, Anushaktinagar, Mumbai 400094, India*
[4] *Key Laboratory of Modern Astronomy and Astrophysics, Nanjing University, Ministry of Education, Nanjing 210023, China*
[5] *Observatorio Astronómico Nacional (OAN-IGN), Spain*

ABSTRACT

Cosmic rays (CRs) have strong influences on the chemistry of dense molecular clouds (MCs). To study the detailed chemistry induced by CRs, we conducted a Yebes W band line survey towards an unshocked MC (which we named as 3C391:NML) associated with supernova remnant (SNR) 3C391. We detected emission lines of 18 molecular species in total and estimated their column densities with local thermodynatic equilibrium (LTE) and non-LTE analysis. Using the abundance ratio $N(\mathrm{HCO^+})/N(\mathrm{CO})$ and an upper limit of $N(\mathrm{DCO^+})/N(\mathrm{HCO^+})$, we estimated the CR ionization rate of 3C391:NML is $\zeta \gtrsim 2.7 \times 10^{-14}$ s^{-1}. However, we caution on adopting this value because chemical equilibrium, which is a prerequisite of using the equations, is not necessarily reached in 3C391:NML. We observed lower $N(\mathrm{HCO^+})/N(\mathrm{HOC^+})$, higher $N(\mathrm{HCS^+})/N(\mathrm{CS})$, and higher $X(l\text{-}\mathrm{C_3H^+})$ by an order of magnitude in 3C391:NML compared with typical values in quiescent dense MCs. We found that enhanced CR ionization rate ($\sim 10^{-16}$ or $\sim 10^{-14}$ s^{-1}) is preferred to reproduce the observation with chemical model. But a more robust estimation of the temperature from observation is crucial to the estimation of CR ionization rate in 3C391:NML.

Keywords: Cosmic rays (329) — Chemical Abundances (224) — Molecular clouds (1072) — Supernova remnants (1667) — Abundance ratios (11)

1. INTRODUCTION

Supernova remnants (SNRs) are believed to be the prime accelerator of cosmic rays (CRs) in our Galaxy (Aharonian 2013). While high-energy CRs ($\gtrsim 280$ MeV) can emit γ-rays through p-p interaction with molecular clouds (MCs), low-energy CRs act as the dominating source of ionization in MCs shielded from UV radiation (Spitzer 1978; Padovani et al. 2009). CR protons can ionize molecular hydrogen through:

$$\mathrm{H_2} \longrightarrow \mathrm{H_2^+} + \mathrm{e^-} \quad (1)$$

followed by:

$$\mathrm{H_2^+} + \mathrm{H_2} \longrightarrow \mathrm{H_3^+} + \mathrm{H}. \quad (2)$$

The $\mathrm{H_3^+}$ ion starts the process of the formation of polyatomic molecular species. Chemical effects of CRs on MCs are not limited to the ionization of $\mathrm{H_2}$. CRs can also drive the transition of CO $\rightarrow$ C $\rightarrow$ $\mathrm{C^+}$ (Bisbas et al. 2017). Other chemical effects of CRs include CR-induced non-thermal desorption (Hasegawa & Herbst 1993), CR-induced UV photons (Sternberg et al. 1987), grain sputtering (Wakelam et al. 2021; Paulive et al. 2022), radiolysis (Shingledecker et al. 2018; Paulive et al. 2021), etc.

Supernova remnants provide an ideal environment to study how CRs affect the chemistry in MCs. Observations have revealed enhanced CR ionization rate ($\sim 10^{-15}$ s^{-1} compared with typical values $\sim 10^{-17}$ s^{-1} (Glassgold & Langer 1974)) in dense MCs associated with SNR W51C (Ceccarelli et al. 2011), W28 (Vaupré et al. 2014; Tu et al. 2024), W44 (Cosentino et al. 2019), and W49B (Zhou et al. 2022). All of these SNRs are in-

ygchen@nju.edu.cn

teracting with MCs and exhibit hadronic γ-ray emission originated from the collision between the high-energy CR protons and H nucleus in the MCs. However, detailed behavior of CR chemistry is seldom studied in the environment of an SNR.

SNR 3C391 is among the prototype SNRs interacting with MCs (Jiang et al. 2010) evidenced by 1720 MHz OH masers (Frail et al. 1996), broadened molecular lines (Reach & Rho 1999, hereafter RR99), and infrared emission from molecules, atoms and ions (e.g. Reach & Rho 1996, 1998, 2000). The OH masers hint enhanced CR ionization rate (Nesterenok 2022). A marginal detection of the 6.4 keV Fe I Kα line was reported by Sato et al. (2014), which is likely the fluorescence produced by interaction between low-energy CRs and dense gas. In the γ-ray band, GeV emission has been detected with Fermi (Ergin et al. 2014), which is also in favor of enhanced CR ionization rate. In addition, an unshocked MC dominated by narrow molecular lines is found outside the shocked cloud (see Figure 6 of RR99 and Figure 1), which provide an excellent site to study the chemical effect of CRs free from the disturbance of the SNR shock wave. Hereafter we refer to this region as 3C391:NML (narrow molecular line) following the nomenclature of RR99 who named the shocked region around the southern 1720 MHz OH maser as 3C391:BML (broad molecular line).

In this paper, we present a new W band (71.5–90 GHz) molecular line survey with the Yebes 40 m radio telescope towards 3C391:NML, aiming at enlarging the sample of SNRs exhibiting enhanced CR ionization rate and investigating the detailed CR chemistry. The paper is organized as follows. We describe the new observation and the archival data in Section 2, and present the observation results in Section 3. In Section 4, we estimate the column densities of detected molecular species, discuss how CRs affect the observed abundances and abundance ratios, and present the result of our chemical simulation. The conclusions are summarized in Section 5.

2. OBSERVATIONS

2.1. *Yebes 40 m observation*

We carried out new pointing observation with the Yebes 40 m radio telescope (PI: Tian-Yu Tu, project code: 23A021) towards 3C391:NML (α_{J2000} = $18^{\rm h}49^{\rm m}24^{\rm s}.13$, δ_{J2000} = $-0°57'58''.17$, see the dashed white circle in Figure 1), which was found by RR99 with narrow-line CS J = 2–1 emission. Position switching mode was adopted throughout the observation with the reference point at α_{J2000} = $18^{\rm h}52^{\rm m}08^{\rm s}$, δ_{J2000} = $-1°09'17''$. The spectral coverage ranged from 71.5 to 90 GHz. The HPBW of the telescope was in a range of

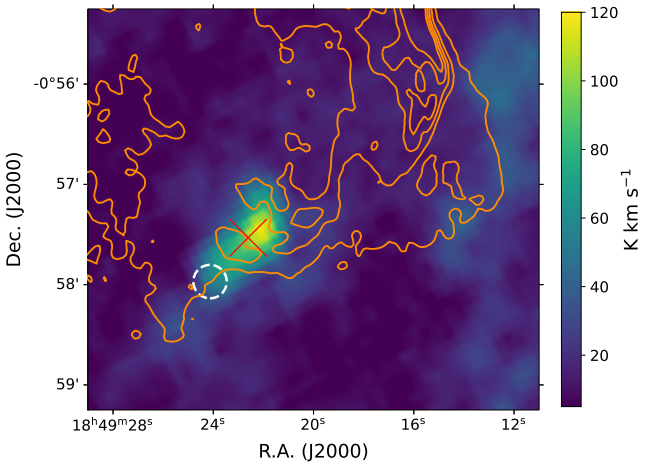

Figure 1. Integrated intensity map of ^{12}CO J = 3–2 line between +100 and +110 km s^{-1} towards the southwestern part of SNR 3C391, overlaid with orange contours of 1.4 GHz radio continuum (levels are 4, 12, 20, 28 and 36 mJy/beam). The red cross shows the 1720 MHz OH maser reported by Frail et al. (1996). The dashed white circle delineates the 3C391:NML region we observed.

$\sim 20''$–$24''$. The data were smoothed to a velocity channel width of 0.2 km s^{-1}, and the resulting sensitivity measured in main beam temperature ($T_{\rm mb}$) is $\approx$ 12–15 mK depending on the frequency. The raw data was reduced with the GILDAS/CLASS package[1].

2.2. *Other archival data*

We used other archival data to support our analysis. We obtained ^{12}CO and ^{13}CO J = 1–0 data from the FUGIN (FOREST Unbiased Galactic plane Imaging survey with the Nobeyama 45-m telescope) project (Umemoto et al. 2017). The angular resolutions are $20''$ for ^{12}CO and $21''$ for ^{13}CO, and the sensitivity estimated in $T_{\rm mb}$ is $\sim$ 1–3 K at a velocity channel width of 0.65 km s^{-1}.

We also obtained ^{12}CO J = 3–2 data from the ^{12}CO (3–2) High-Resolution Survey (COHRS) project (Park et al. 2023). The angular resolution is $16.6''$ and the sensitivity measured in $T_{\rm A}^*$ is $\sim$ 1 K at a velocity channel width of 0.635 km s^{-1}. The antenna temperature was converted to $T_{\rm mb}$ with a main beam efficiency of 0.61. We smoothed the data to an angular resolution of $20''$ which is similar to the beam of the FUGIN data and our Yebes data.

Supplementary VLA 1.4 GHz radio continuum map was taken from the SNRcat[2] (Ferrand & Safi-Harb 2012). All the processed data were further analyzed with *Python* packages Astropy (Astropy Collaboration

[1] https://www.iram.fr/IRAMFR/GILDAS/

[2] http://snrcat.physics.umanitoba.ca

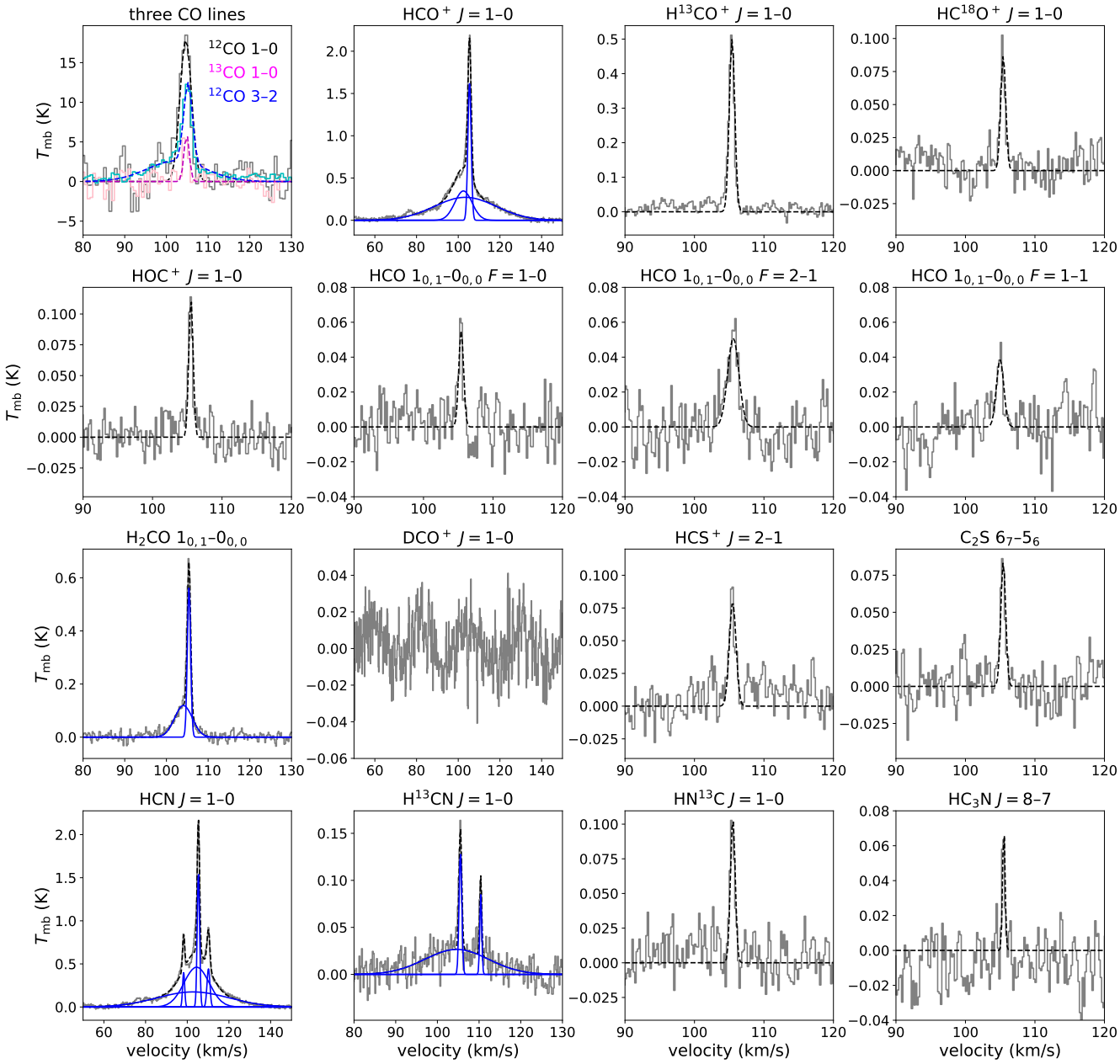

Figure 2. The spectra of detected molecular lines by the Yebes 40 m observation, as well as the spectra of three CO lines and the non-detection of DCO$^+$ J = 1–0 line. For the CO lines, the solid grey, pink and cyan lines show the ^{12}CO J = 1–0, ^{13}CO J = 1–0, and ^{12}CO J = 3–2 lines, respectively, while the dashed black, magenta and blue lines show the results of (multi-)Gaussian fitting to the ^{12}CO J = 1–0, ^{13}CO J = 1–0, and ^{12}CO J = 3–2 lines, respectively. For other molecular transitions, the grey lines shows the observed spectra, the black lines shows the fitting results, and the blue lines shows the components if multi-Gaussian fitting is adopted. The ranges of the local-standard-of-rest (LSR) velocity are adjusted for better visualization.

et al. 2018, 2022) and Spectral-cube (Ginsburg et al. 2015). The data cubes of the CO isotopes were reprojected with Montage[3] package. We visualized the data with *Python* package Matplotlib[4].

[3] http://montage.ipac.caltech.edu/

[4] https://matplotlib.org/

3. RESULTS

In Figures 2 and 3 we display the spectra of all the molecular lines detected by the Yebes 40 m observation, as well as the spectra of three CO lines and the non-detection of DCO$^+$ J = 1–0 line. We detected 18 species (including isotopes) in total, some of which are seldom studied in the environment of SNRs.

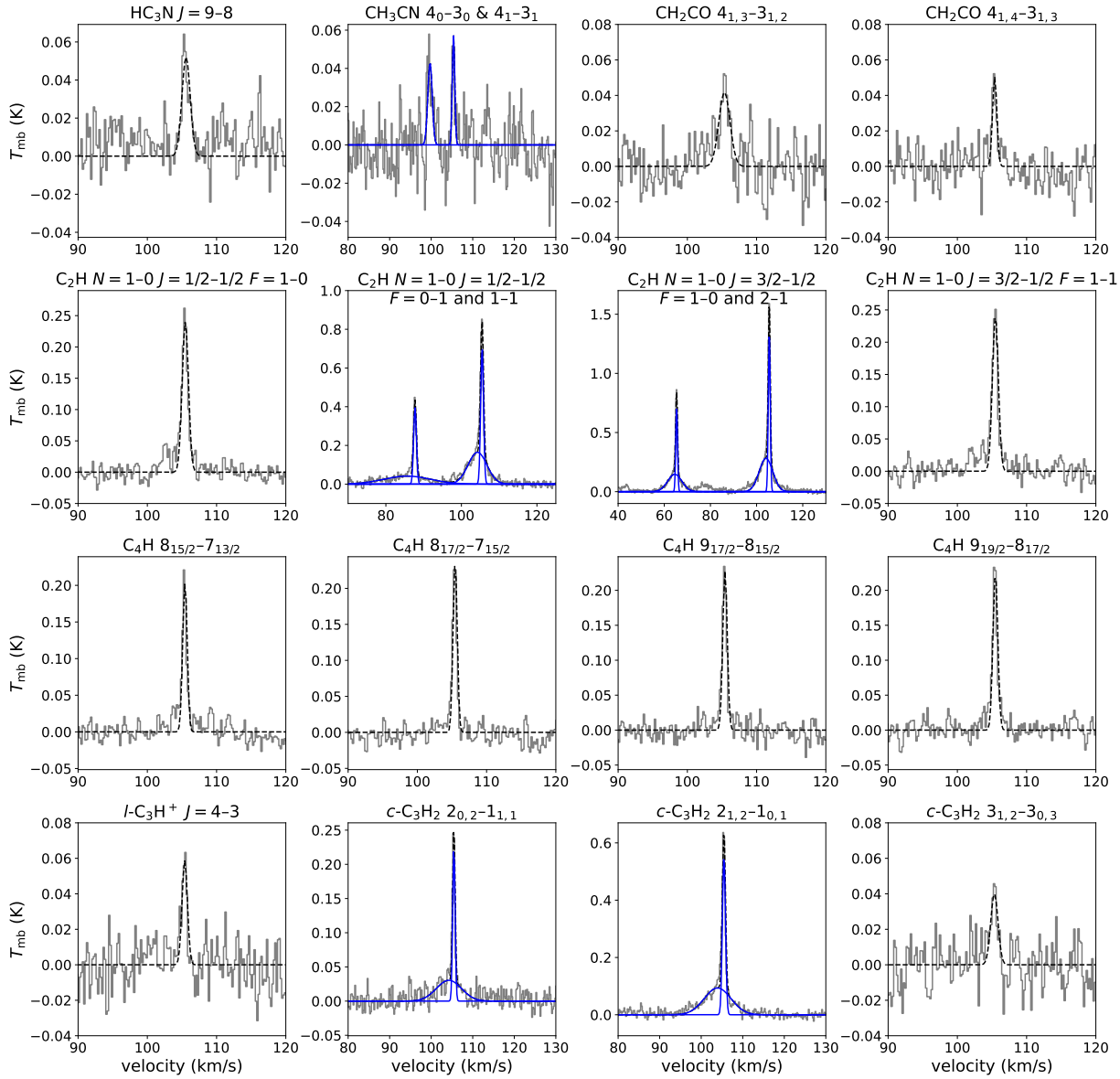

Figure 3. Same as Figure 2 but for different species.

Also shown in Figure 2 and 3 are the results (multi-)Gaussian fitting to the spectra. All of the detected species show narrow line emission centered at $V_{\rm LSR} \approx$ 105.5 km/s, consistent with the results of RR99. The fitted $T_{\rm peak}$ and FWMH of the narrow components are summarized in Table 2.

We find three components in the spectrum of HCO^+ (see Figure 2): a narrow line centered at 105.4 km s^{-1}, a moderately broadened component centered at 102.5 km s^{-1} with an FWHM of 9.7 km s^{-1}, and a very broad component centered at 103.4 km s^{-1} with an FWHM of 34.8 km s^{-1}. The moderately broadened component has been reported by RR99, but the broadest component is detected for the first time. These two broadened components may be the results of the shock of SNR propagating into different layers of 3C391:NML. In the outer layer, the velocity of the shock is high, resulting in a large linewidth, while the opposite when the shock wave goes deeper into the cloud. Detailed analysis of the shocked components is beyond the scope of this study.

Similar line profile is also found in the spectra of HCN J = 1–0 line, but two peaks can be seen in the blue and red sides of the main peak. These are the hyperfine structures (HFS) located at -7.1 km s^{-1} and $+4.9$ km s^{-1} relative to the main component. Spectra consisting of two components, including a narrow one and a moderately broadened one, were detected in ^{12}CO J = 3–2, H_2CO $1_{0,1}$–$0_{0,0}$, $H^{13}CN$ J = 1–0, four lines of C_2H, and two lines of c-C_3H_2.

In the following contents, we mainly focus on the narrow component because it is supposed to be free from the disturbance of the SNR shock wave. We note that RR99 found the $T_{\rm peak}$ of the narrow component of HCO^+ is 1.0 K, which is smaller than the fitted value shown in Table 2. This is because the beam size of their observation is 27″, which is larger than our 20″ beam. Using these two values, we can estimate that the angular size of the MC emitting narrow line is ≈ 21″. Therefore, we assume the beam filling factor is unity in the following discussions.

4. DISCUSSION

4.1. *Estimation of molecular column density*

4.1.1. *Non-LTE estimation*

To estimate the column densities of different molecular species of the unshocked component, we first use SpectralRadex[5], which is a *Python* wrapper of the radiative transfer code, RADEX (van der Tak et al. 2007), to present non-LTE (local thermodynamical equilibrium) analysis. The collisional coefficients are taken from LAMDA[6] (Leiden Atomic and Molecular Database) (van der Tak et al. 2020). The geometry of the emitting object is chosen to be sphere. We assume a kinetic temperature $T \approx 20$ K, consistent with the value adopted by RR99 and the temperature estimated from the line ratio $I(\rm H^{13}CN)/I(\rm HN^{13}C)$ (Pazukhin et al. 2022), which is ≈ 23 K in our case. The analysis is conducted with CO, *o*-*c*-C_3H_2, and CS. The data of CS emission lines are obtained from the results of RR99. We run a grid of density ($n_{\rm H_2}$) and column density (N) of specific molecular species and find the best-fit values for each species. The results are shown in Figure 4 and Table 1.

For CO, we use the ^{12}CO 1–0, ^{13}CO 1–0 and ^{12}CO 3–2 lines for the analysis, and we fit the ratios $T_{\rm mb}(^{12}\rm CO\ 3\text{–}2)/T_{\rm mb}(^{12}\rm CO\ 1\text{–}0)$ and $T_{\rm mb}(^{12}\rm CO\ 3\text{–}2)/T_{\rm mb}(^{13}\rm CO\ 1\text{–}0)$. We assume $N(^{12}\rm CO)/N(^{13}\rm CO) = 45$ in our calculation (Milam et al. 2005). The best-fit values, marked by the intersection point of the two solid lines in the upper left panel of Figure 4, are $N(^{12}\rm CO) \sim 3.7 \times 10^{17}$ cm^{-2} and $n_{\rm H_2} \sim 1.4 \times 10^3$ cm^{-3}. We note that there is parameter degeneracy in our fitting, so the values are just a rough estimation.

For *o*-*c*-C_3H_2, we use the *o*-*c*-C_3H_2 $3_{1,2}$–$3_{0,3}$ and $2_{1,2}$–$1_{0,1}$ lines, and fit the $T_{\rm mb}(3_{1,2}\text{–}3_{0,3})/T_{\rm mb}(2_{1,2}\text{–}1_{0,1})$ ratio and $T_{\rm mb}(2_{1,2}\text{–}1_{0,1})$. The best-fit values are N(*o*-*c*-C_3H_2) $\sim 2.0 \times 10^{12}$ cm^{-2} and $n_{\rm H_2} \sim 2.4 \times 10^5$ cm^{-3}

[5] https://spectralradex.readthedocs.io/en/latest/

[6] https://home.strw.leidenuniv.nl/~moldata/

Table 1. Results of non-LTE analysis of CO, *o*-*c*-C_3H_2, and CS lines.

Species	Column density (cm^{-2})	$n_{\rm H2}$ (cm^{-3})
CO	$\sim 3.7 \times 10^{17}$	$\sim 1.4 \times 10^3$
o-*c*-C_3H_2	$\sim 2.0 \times 10^{12}$	$\sim 2.4 \times 10^5$
CS (20 K)	$\sim 3.9 \times 10^{12}$	$\sim 1.9 \times 10^5$
CS (40 K)	$\sim 3.9 \times 10^{12}$	$\sim 1.0 \times 10^5$

For CS, we fit $T_{\rm mb}$(CS 3–2)/$T_{\rm mb}$(CS 2–1) and $T_{\rm mb}$(CS 2–1), and use the non-detection of CS 5–4 reported by RR99 as an upper limit. The best-fit values are $N(\rm CS) \sim 3.9\times10^{12}$ cm^{-2} and $n_{\rm H_2} \sim 1.9\times10^5$ cm^{-3}. We also show the fitting results of CS assuming $T = 40$ K in the lower right panel of Figure 4. The results shows that the kinetic temperature of 3C391:NML should not be much higher than 40 K, otherwise the CS 5–4 line should have been detected. The CS lines set an upper limit for the kinetic temperature T. We also note that although the kinetic temperatures are different, the best-fit N(CS) does not change significantly, and the variation of the corresponding excitation temperature of CS 2–1 line (≈ 10 K) is also not prominent. This excitation temperature will be used to conduct LTE analysis for the other species in the following section.

The densities estimated with the *o*-*c*-C_3H_2 and CS lines are similar and higher respectively than that estimated with CO. This is not surprising because the critical densities are $\sim 10^6$ cm^{-3} for the *o*-*c*-C_3H_2 and CS lines, while $\sim 10^3$–10^4cm^{-3} for the CO lines, which means that *o*-*c*-C_3H_2 and CS trace a denser part of the MC than CO.

For other molecular species, non-LTE analysis is not available. We use LTE analysis to estimate their column densities.

4.1.2. *LTE estimation*

We assume LTE condition for the molecular species other than CO, *o*-*c*-C_3H_2, and CS analyzed above Assuming the lines to be optical thin, we obtain the column densities through (Equation C1 in Liu et al. (2021)):

$$N = \frac{3k}{8\pi^3\nu}\frac{Q_{\rm rot}\exp\left(E_{\rm u}/kT_{\rm ex}\right)}{S\mu^2} \times \frac{J_\nu(T_{\rm ex})}{J_\nu(T_{\rm ex}) - J_\nu(T_{\rm bg})}\int T_{\rm mb}\,dv, \quad (3)$$

where $Q_{\rm rot}$ is the partition function, $E_{\rm u}$ is the energy of the upper level, $T_{\rm ex}$ is the excitation temperature, S is

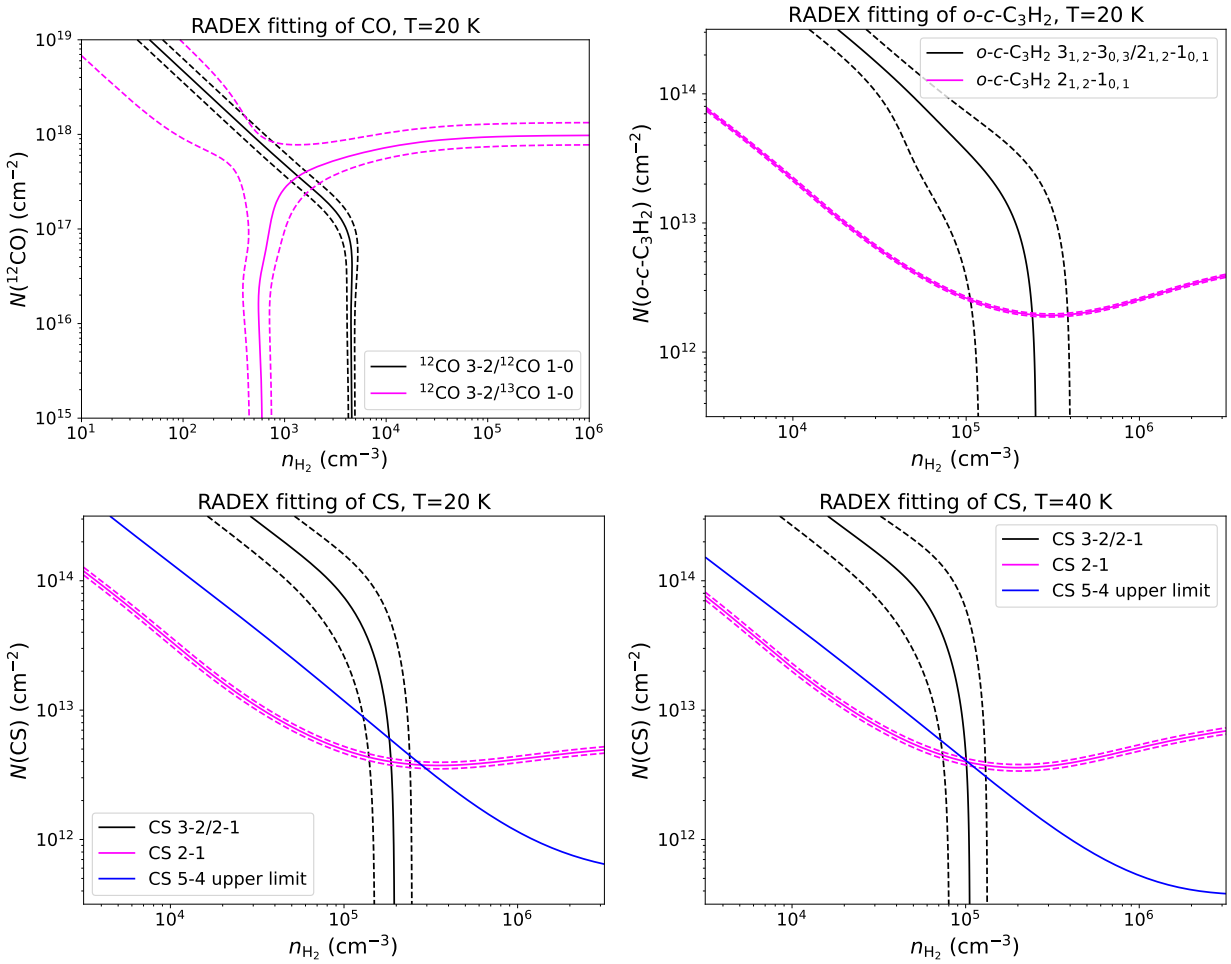

Figure 4. Results of the non-LTE analysis with SpectralRadex. The solid contours show the observed $T_{\rm mb}$ or $T_{\rm mb}$ ratios of lines, while the dashed lines are the estimated uncertainties of the observed values. *(upper left)* Results of CO with $T = 20$ K. The black contours show ^{12}CO 3–2/^{12}CO 1–0. The magenta contours show ^{12}CO 3–2/^{13}CO 1–0. *(upper right)* Results of o-c-C_3H_2 with $T = 20$ K. The black contours show o-c-C_3H_2 $3_{1,2}$–$3_{0,3}$/$2_{1,2}$–$1_{0,1}$. The magenta contours show the $2_{1,2}$–$1_{0,1}$ line. *(lower left)* Results of CS with $T = 20$ K. The black contours show CS 3–2/2–1. The magenta contours show CS 2–1. The blue contour shows the upper limit of CS 5–4. *(lower right)* Same as the lower left panel but for $T = 40$ K.

the line strength, μ is the dipole moment, $T_{\rm bg} = 2.73$ K is the background temperature, and $J_\nu(T)$ is defined by $J_\nu(T) = (h\nu/k)/(\exp(h\nu/kT) - 1)$. We adopt the $Q_{\rm rot}$, $E_{\rm u}$ and $S\mu^2$ from Splatalogue[7]. The data of HCO are extracted from the JPL database[8], while other data are from the CDMS database[9].

We use two values of $T_{\rm ex}$ (5 K and 10 K) to estimate the column density for each molecular species, which are tabulated in Table 2. $T_{\rm ex}$ is calculated with the following two methods. (1) The optical depth of HCO^+ can be obtained by solving:

$$\frac{1 - {\rm e}^{-\tau}}{1 - {\rm e}^{-\tau/327}} = \frac{W({\rm HCO^+})}{W({\rm HC^{18}O^+})}, \quad (4)$$

where W is the integrated intensity and we assume $N({\rm HCO^+})/N({\rm HC^{18}O^+}) \approx N^{16}{\rm O}/N^{18}{\rm O} \approx 327$ (Yan et al. 2023) considering the galactocentric distance of 3C391 is ≈ 4.4 kpc (Ranasinghe & Leahy 2022). We get $\tau \approx 8$, which is high enough for us to estimate the excitation temperature of HCO^+ by (Mangum & Shirley 2015):

$$T_{\rm ex} = \frac{h\nu/k}{\ln\left(1 + \frac{h\nu/k}{T_{\rm peak}/f + J_\nu(T_{\rm bg})}\right)}. \quad (5)$$

Then we get $T_{\rm ex} = 5$ K for HCO^+. We adopt this value as a first estimation of $T_{\rm ex}$. (2) According to the results of RADEX (in Section 4.1.1), the excitation temperature of the CS 2–1 line is ≈ 10 K. We adopt this value as the second estimation of $T_{\rm ex}$.

[7] https://splatalogue.online/
[8] https://spec.jpl.nasa.gov/
[9] https://cdms.astro.uni-koeln.de/

Equation 3 only applies when the transition is optical thin which is, however, not necessarily satisfied in some of the detected lines. To minimize the influence of finite optical depth, we use the emission from rarer isotopes or the HFS to calculate the column density when isotopes or HFS are detected. Specifically, we use $HC^{18}O^+$ to calculate $N(HCO^+)$, $H^{13}CN$ for $N(HCN)$, and C_2H $N = 1$–0 $J, F = 3/2, 1$–$1/2,1$ for $N(C_2H)$. For C_4H, the results estimated with the two 8–7 lines (or the two 9–8 lines) are similar, but there is a significant difference between the values estimated by 8–7 and 9–8 lines. For HCO, HC_3N, CH_2CO and CH_3CN, although multiple transitions are detected, we calculate the column densities with all detected transitions because they are rather weak and the results are different.

As seen in Table 2, for most species, the column densities estimated with the two different T_{ex} are consistent within a factor of 2, except HC_3N, C_4H, CH_2CO and CH_3CN. For HC_3N, CH_2CO and CH_3CN, there is also a non-negligible difference between the estimated column densities with different transitions, probably because the lines are rather weak and the relative uncertainty is high.

4.2. *Relation between the observed molecular abundances and CR chemistry*

In Section 4.1.1, we obtained the $N(^{12}CO) \sim 3.7 \times 10^{17}$ cm^{-2}. Assuming $N(H_2) \approx 7 \times 10^5 N(^{13}CO)$ (Frerking et al. 1982), we obtain $N(H_2) \sim 5.8 \times 10^{21}$ cm^{-2}. We will use this value to estimate the molecular abundance relative to H_2.

4.2.1. *Estimation of CR ionization rate with analytic method*

The abundance ratios $R_D = N(DCO^+)/N(HCO^+)$ and $R_H = N(HCO^+)/N(CO)$ has been used to estimate the CR ionization rate in MCs (Caselli et al. 1998; Ceccarelli et al. 2011; Vaupré et al. 2014). Assuming the chemistry of 3C391:NML has reached equilibrium and the temperature is low ($\ll 220$ K), the CR ionization ζ can be calculated simply with (Vaupré et al. 2014):

$$\begin{aligned} \frac{\zeta}{n_H} &= \frac{\beta'}{k_H}\left(2\beta x_e + \delta\right) R_H x_e, \\ x_e &= \left(\frac{k_f x(HD)}{3R_D} - \delta\right)\frac{1}{k_e} \end{aligned} \tag{6}$$

where x_e is the ionization fraction in the MC, $x(HD)$ is the abundance of HD relative to H, k_f, δ, β and β' are rate coefficients of chemical reactions listed in the Table A.1. of Vaupré et al. (2014). These equations allow us to set a lower limit for ζ even though DCO^+ is not detected. Assuming $x(HD) = 1.6 \times 10^{-5}$ (Linsky et al. 2006) and adopting $n_H = 2.8 \times 10^3$ cm^{-3} from the non-LTE analysis of CO, we get $\zeta \gtrsim 2.7 \times 10^{-14}$ s^{-1}. This value is higher than the typical value in MCs ($\sim 10^{-17}$ s^{-1} Glassgold & Langer 1974) by three orders of magnitude, and the values obtained in W51C and W28 with the same method by one order of magnitude (Ceccarelli et al. 2011; Vaupré et al. 2014).

We note, however, that chemical equilibrium is not necessarily reached in 3C391:NML. Although the timescale of gas-phase ion-neutral reactions induced by CRs is only $\sim 10^2$ yr (Vaupré et al. 2014), grain chemistry may take longer time to reach equilibrium. The deuterium chemistry is strongly affected by grain processes (e.g., Feng et al. 2020). We recall that the rate coefficient of CR-induced non-thermal desorption for a specific grain species is (Hasegawa & Herbst 1993):

$$k_{CR} = f(70\text{ K})k_{des}(70\text{ K}), \tag{7}$$

where $f(70$ K$)$ is the fraction of the time spent by dust grains at the dust temperature $T_{dust} = 70$ K due to CR heating, which is approximately (Reboussin et al. 2014):

$$f(70\text{ K}) = \frac{\zeta}{1.3 \times 10^{-17}\text{ s}^{-1}} 3.16 \times 10^{-19}. \tag{8}$$

The value $k_{des}(70$ K$)$ is the rate coefficient of thermal desorption rate at $T_{dust} = 70$ K, which can be expressed as:

$$k_{des} = \nu_0 \exp\left(-\frac{E_D}{kT_{dust}}\right), \tag{9}$$

where E_D is the desorption energy of the adsorbed species, and

$$\nu_0 = \left(\frac{2n_s E_D}{\pi^2 m}\right)^{1/2}, \tag{10}$$

where $n_s \sim 1.5 \times 10^{15}$ cm^{-2} is the surface density of sites and m is the mass of the adsorbed species. For CO, the desorption energy is ≈ 1200 K (Hasegawa & Herbst 1993). Substituting the values into these equations, we estimate that the CR-induced non-thermal desorption timescale for CO ice at $\zeta \sim 10^{-14}$ s^{-1} is $\tau_{CR} \approx 1/k_{CR} \sim 3 \times 10^3$ yr, which is comparable to the age of SNR 3C391 (4–19 kyr. See our further discussion in Section 4.2.3). We note that k_{CR} depends exponentially on the desorption energy E_D (see Equation 9) which varies with species. A substantial proportion of ice is composed of H_2O, NH_3, CH_3OH etc. (Ruaud et al. 2016). These species have higher values of E_D, which result in longer desorption timescale. Therefore, the chemistry may be highly dynamic in the environment of 3C391, and the CR ionization rate estimated with Equations 6 may thus deviate from the real value.

Table 2. Results from Gaussian fitting of the narrow line components of all detected lines in the Yebes 40 m observation, as well as the column densities of molecular species.

Species	Transition	Frequency (MHz)	$T_{\rm peak}$ (K)	FWHM (km s^{-1})	$N(T_{\rm ex}=5$ K)[a] (cm^{-2})	$N(T_{\rm ex}=10$ K)[a] (cm^{-2})
HCO^+	1–0	89188.525	1.62	1.87	3.3(13) for HCO^+[b]	2.9(13) for HCO^+[b]
$H^{13}CO^+$	1–0	86754.288	0.50	0.93		
$HC^{18}O^+$	1–0	85162.223	0.087	0.74		
DCO^+	1–0	72039.312	< 0.045[c]	—	$< 7.7(10)$	$< 7.1(10)$
HCN	1–0 $F=0$–1	88633.936	0.40	1.16	1.5(13) for HCN[d]	1.3(13) for HCN[d]
	1–0 $F=2$–1	88631.847	1.54	1.36		
	1–0 $F=1$–1	88630.416	0.44	1.63		
$H^{13}CN$	1–0 $F=1$–1	86338.737	0.085	0.56		
	1–0 $F=2$–1	86340.176	0.13	0.77		
$HN^{13}C$	1–0	87090.859	0.10	0.81	1.8(11)	1.6(11)
HOC^+	1–0	89487.414	0.11	0.73	2.1(11)	1.9(11)
HCO	$1_{0,1}$–$0_{0,0}$					
	$J,F=3/2,1$–$1/2,0$	86708.35	0.056	0.80	1.2(12)	2.0(12)
	$J,F=3/2,2$–$1/2,1$	86670.82	0.050	1.96	1.6(12)	2.5(12)
	$J,F=1/2,1$–$1/2,1$	86777.43	0.038	1.28	1.4(12)	2.2(12)
H_2CO	$1_{0,1}$–$0_{0,0}$	72837.951	0.57	0.93	3.5(12)	5.5(12)
HCS^+	2–1	85347.869	0.080	1.13	6.9(11)	5.4(11)
HC_3N	8–7	72783.818	0.075	0.41	5.9(11)	1.7(11)
	9–8	81881.463	0.052	1.40	2.4(12)	4.6(11)
C_2H	$N=1$–0				1.9(14)	1.7(14)
	$J,F=1/2,1$–$1/2,0$	87446.512	0.24	1.08		
	$J,F=1/2,0$–$1/2,1$	87407.165	0.39	0.88		
	$J,F=1/2,1$–$1/2,1$	87402.004	0.70	0.89		
	$J,F=3/2,1$–$1/2,0$	87328.624	0.70	0.92		
	$J,F=3/2,2$–$1/2,1$	87316.925	1.34	0.99		
	$J,F=3/2,1$–$1/2,1$	87284.156	0.24	1.01		
C_2S	6_7–5_6	81505.208	0.086	0.80	1.6(12)	8.8(11)
C_4H	$8_{17/2}$–$7_{15/2}$	76117.43	0.23	0.73	4.3(13)	1.1(13)
	$8_{15/2}$–$7_{13/2}$	76156.02	0.20	0.77		
	$9_{19/2}$–$8_{17/2}$	85634.00	0.22	0.81	8.3(13)	1.5(13)
	$9_{17/2}$–$8_{15/2}$	85672.57	0.23	0.76		
l-C_3H^+	4–3	89957.625	0.067	0.75	3.5(11)	1.7(11)
o-c-C_3H_2	$3_{1,2}$–$3_{0,3}$	82966.201	0.041	1.22	2.0(12)[e]	
	$2_{1,2}$–$1_{0,1}$	85338.906	0.56	0.87		
p-c-C_3H_2	$2_{0,2}$–$1_{1,1}$	82093.555	0.23	0.68	3.7(12)	3.6(12)
CH_2CO	$4_{1,3}$–$3_{1,2}$	81586.229	0.041	1.92	1.7(13)	4.2(12)
	$4_{1,4}$–$3_{1,3}$	80076.644	0.051	0.74	8.1(12)	2.0(12)
CH_3CN	4_1–3_1	73588.799	0.056	0.71	9.4(11)	3.1(11)
	4_0–3_0	73590.217	0.044	1.19	2.8(11)	1.9(11)

NOTE— [a] m(n) means m$\times 10^{\rm n}$. [b] The column density of HCO^+ is estimated from $HC^{18}O^+$ assuming $N(HCO^+)/N(HC^{18}O^+) \approx {}^{16}O/{}^{18}O \approx 327$ (Yan et al. 2023). [c] DCO^+ is not detected, so we use the 3σ value as an upper limit. [d] The column density of HCN is estimated from $H^{13}CN$ assuming $N(HCN)/N(H^{13}CN) \approx {}^{12}C/{}^{13}C \approx 45$ (Milam et al. 2005). [e] The column density of o-c-C_3H_2 is estimated with non-LTE method (see Section 4.1.1).

4.2.2. *Unusual abundance and abundance ratios found by the Yebes observation*

Using the column densities listed in Table 2 and the estimated $N(H_2) \sim 5.8 \times 10^{21}$ cm^{-2}, we can obtain the abundances of the detected species. We find that the obtained $N(HCO^+)/N(HOC^+)$, $N(HCS^+)/N(CS)$ and $X(l\text{-}C_3H^+)$ are different from typical values found in dense MCs. Here X denotes the abundance of a specific species relative to H_2. All of the three values can probably be attributed to the chemistry of CRs.

The observed value of $N(HCO^+)/N(HOC^+)$ is $\sim$ 160–180, while typical value found in quiescent dense MCs in our Galaxy is $\sim 10^3$ (Apponi & Ziurys 1997), which is higher than our observed value by an order of magnitude. The low $N(HCO^+)/N(HOC^+)$ has been found in Galactic photodissociation regions (PDRs) (e.g. the Horsehead PDR (Goicoechea et al. 2009) and Orion Bar PDR (Goicoechea et al. 2017)), diffuse clouds (Liszt et al. 2004), and extragalactic sources (e.g. NGC 253 (Harada et al. 2021) and M 82 (Fuente et al. 2008)). In low-temperature molecular gas, Harada et al. (2021) proposed that the decrease $N(HCO^+)/N(HOC^+)$ at high visual extinction A_V gas shielded from UV radiation is caused by the extremely high CR ionization rate $\sim 10^{-14}$ s^{-1} in the central molecular zone (CMZ) of NGC 253. In this case, the reduction of $N(HCO^+)/N(HOC^+)$ is due to the enrichment of C^+ and CO^+, which in turn leads to a faster production of HOC^+ through reactions:

$$\begin{aligned} C^+ + H_2O &\longrightarrow HOC^+ + H \\ &\longrightarrow HCO^+ + H \end{aligned} \tag{11}$$

with a branching ratio of 2:1, and

$$\begin{aligned} CO^+ + H_2 &\longrightarrow HOC^+ + H \\ &\longrightarrow HCO^+ + H \end{aligned} \tag{12}$$

with a branching ratio of 1:1.

The observed value of $N(HCS^+)/N(CS)$ is $\sim$ 0.14–0.18, while the typical values found in the Taurus, Perseus, Orion MCs and Barnard 1 dark cloud are all $\sim 10^{-2}$ (Rodríguez-Baras et al. 2021; Fuente et al. 2016), which is lower than our observed value by an order of magnitude. The chemical simulation of Fuente et al. (2016) shows that the enhanced $N(HCS^+)/N(CS)$ ratio could be a tracer of high CR ionization rate at chemical equilibrium, because H_3^+, HCO^+, and H_3O^+, which are all important products of CR ionization, are important reactants that transform CS to HCS^+ (Podio et al. 2014). Though, this simulation considered only a narrow range of CR ionization rate and is limited to chemical equilibrium.

The observed value of $X(l\text{-}C_3H^+)$ is ~ 2.9–6.0×10^{-11}. The $l\text{-}C_3H^+$ molecular species is first discovered in the Horsehead PDR (Pety et al. 2012), and Guzmán et al. (2015) proposed that the high abundance of $l\text{-}C_3H^+$ ($\sim 10^{-11}$) in the Horsehead is due to the PDR chemistry which produces abundant C^+ ions and possibly the photo-erosion of PAHs. Gerin et al. (2019) found that $l\text{-}C_3H^+$ is ubiquitous in diffuse gas, with an abundance of $\sim 7 \times 10^{-11}$. The first detection of $l\text{-}C_3H^+$ in quiescent dense MC is reported by Cernicharo et al. (2022) who found $X(C_3H^+) \sim 2.4 \times 10^{-12}$ in the TMC-1 cloud. This value is lower than our observed value by an order of magnitude.

We note that the visual extinction of 3C391:NML is $A_V \approx 6.2$ assuming $N_H/A_V = 1.87 \times 10^{21}$ cm^{-2} mag^{-1} (Bohlin et al. 1978). In addition, we do not find any source of strong UV radiation close to the MC in the SIMBAD database[10] (Wenger et al. 2000). Therefore, the chemistry of 3C391:NML is not likely to be dominated by UV photons (Wolfire et al. 2022). On the other hand, CRs, which can enhance the abundances of ionized species like C^+, H_3^+, CO^+ and H_3O^+, may provide advantages to explain the observed abundance and abundance ratios.

4.2.3. *Results of chemical simulation*

To further investigate the chemistry and constrain the cosmic-ray (CR) ionization rate in our target MC, we present a chemical simulation using the `DNautilus 2.0` chemical code (Taniguchi et al. 2024). This code represents an updated version of `DNAUTILUS.1.0` as introduced in Majumdar et al. (2017). It is capable of simulating time-dependent abundances in two phase (treating the entire grain as homogeneous) and three phase (making a distinction between the surface and bulk of the grain).

In `DNautilus 2.0`, deuteration is achieved up to the 14th largest atom-based molecule present in the kida.uva.2014 network, which is available in the KIDA database[11]. The deuteration routine used is described in Albertsson et al. (2013), resulting in 1606 gas species, 1472 grain-surface species, and 1472 grain-mantle species. These are connected by 83,715 gas-phase reactions, 10,967 reactions on grain surfaces, and 9,431 reactions in the grain mantles in `DNautilus 2.0`.

The simulation consists of two steps. In step 1, we simulate the chemistry of a dense MC with low CR ionization rate per H_2 ($\zeta = 10^{-17}$ s^{-1}) and low gas temperature $T = 10$ K for $t_1 = 0.1$ Myr and 1 Myr to mimic the

[10] https://simbad.u-strasbg.fr/simbad/

[11] https://kida.astrochem-tools.org/

Table 3. Physical parameters for step 1 and step 2

Parameter	Value used in step 1	Value used in step 2
t_1 (Myr)	0.1, 1	—
T (K)	10	10–50
$n_{\rm H}$ (cm^{-3})	2×10^3–2×10^6	2×10^3–2×10^6
$\log_{10}(\zeta/s^{-1})$	−17	−17, −16, −15, −14
C/O ratio	0.6, 0.8, 1.0, 1.2	0.6, 0.8, 1.0, 1.2

chemical evolution of the MC before the supernova explosion. A grid of density $n_{\rm H}$ (10 values between 2×10^3 and 2×10^6 cm^{-3}) and C/O element ratio (0.6, 0.8, 1.0 and 1.2) is explored in step 1. Initially, all the abundances are in elemental form except for hydrogen and deuterium which appear in molecular form as H_2 and HD, respectively. Elements whose ionization potentials are less than 13.6 eV such as C, S, Si, Fe, Na, Mg, Cl and P appear in their first ionization states. In step 2, we use the results of step 1 as input abundances, keep the density and the C/O ratio constant, and vary ζ (10^{-17}, 10^{-16}, 10^{-15} and 10^{-14} s^{-1}) and T (10 values between 10 and 50 K) to mimic the impact of CRs after the supernova explosion. The physical parameters that are explored are listed in table 3. The initial elemental abundances for step 1 are shown in Table 4 and the initial abundances of H_3^+, H_2D^+, HCO^+, $DCO^+$and CO for step 2 for C/O ratio 0.8 in Table 5.

The evolution time for step 2 is chosen according to the age of 3C391. With various scenarios such as Sedov evolution, cloud evaporation, and radiative phase, the age of SNR 3C391 was estimated within a range between 4-19 kyr (Reynolds & Moffett 1993; Rho & Petre 1996; Chen & Slane 2001; Chen et al. 2004; Leahy & Ranasinghe 2018). We extract the abundances of the species in step 2 at 8000 yr, which is an intermittent value. The results of the simulation are shown in Figure 5 for $t_1 = 0.1$ Myr and Figure 6 for $t_1 = 1$ Myr. We note that the difference in results with different C/O ratio is negligible. So we only show the results with C/O = 0.8 as a representative in Figures 5 and 6. The difference between the results with $t_1 = 0.1$ and 1 Myr is due to the different depletion level in step 1, and thus the different initial condition in step 2.

The simulation fails to reproduce the observed values of $N(HCS^+)/N(CS)$ (0.14–0.18), with typical simulated values $\lesssim 10^{-2}$ in any combination of parameters. This is understandable as Sulphur chemistry is poorly understood in astrochemical environments (Vidal et al. 2017). So we do not show the results here.

Table 4. Initial elemental abundances for step 1

Element	Abundance relative to H
H_2	0.50
He	9.00(−2)
N	6.20(−5)
O	(2.83, 2.12, 1.70, 1.41)(−4)
C^+	1.70(−4)
S^+	8.00(−8)
Si^+	8.00(−8)
Fe^+	3.00(−9)
Na^+	2.00(−9)
Mg^+	7.00(−9)
P^+	2.00(−10)
Cl^+	1.00(−9)
F	6.68(−9)
HD	1.60(−5)

The three abundance ratios are all related to the molecule HCO^+. The formation of HCO^+ is mainly through:

$$CO + H_3^+ \longrightarrow HCO^+ + H_2 \qquad (13)$$

in most of the physical conditions whereas the formation reactions of HOC^+ including reactions (11) and (12) depend on the specific value of ζ, $n_{\rm H}$ and T. The major production and destruction pathways of HCO^+ and HOC^+ are listed in Table 6. We note that the abundance ratio $N(HCO^+)/N(HOC^+)$ exhibits a rather regular dependency on different physical parameters at $T \lesssim 40$ K—decreased with higher ζ and lower $n_{\rm H}$, while decreased with higher T. We therefore propose that the low $N(HCO^+)/N(HOC^+)$ abundance ratio may be a good tracer of enhanced CR ionization rate in dark unshocked cloud associated with SNRs if other physical parameters are well constrained by observation.

The molecule l-C_3H^+, as a carbon chain species, is expected to be sensitive to the C/O ratio (e.g., Pratap et al. 1997). However, we find that the dependence of $X(l\text{-}C_3H^+)$ on the C/O ratio is not very significant, which is also reported by Loison et al. (2014), and does not affect our conclusions.

We note that the $X(l\text{-}C_3H^+)$ is higher when the CR ionization rate is higher.

Table 5. Relative abundance of some molecules w.r.t H for step 2 for C/O ratio = 0.8

t_1 (Myr)	n_H (cm^{-3})	H_3^+	H_2D^+	HCO^+	DCO^+	CO
0.1	2×10^3	2.41(−9)	7.70(−11)	1.53(−9)	1.50(−11)	3.28(−5)
	2×10^4	2.59(−10)	1.17(−11)	3.55(−10)	2.67(−12)	4.62(−5)
	2×10^5	7.58(−10)	8.55(−10)	8.96(−11)	1.26(−10)	4.11(−7)
	2×10^6	2.14(−10)	2.89(−10)	1.85(−12)	2.94(−12)	7.90(−9)
1.0	2×10^3	4.90(−9)	3.02(−10)	7.55(−9)	2.10(−10)	7.34(−5)
	2×10^4	7.20(−9)	2.88(−9)	4.72(−10)	1.34(−10)	1.27(−6)
	2×10^5	4.07(−9)	1.14(−9)	3.76(−11)	5.29(−12)	7.50(−8)
	2×10^6	1.36(−9)	3.39(−10)	3.98(−12)	3.76(−13)	7.57(−9)

Table 6. Major Chemical Reactions for HCO^+, HOC^+, DCO^+, and CO

Species	**Production Reactions**	**Destruction Reactions**
HCO^+	$CO + H_3^+ \rightarrow H_2 + HCO^+$	$HCO^+ + e^- \rightarrow H + CO$ $HCN + HCO^+ \rightarrow CO + HCNH^+$ ($\zeta \lesssim 10^{-16}$ s^{-1} and $T \gtrsim 43$ K)
HOC^+	$CO + H_3^+ \rightarrow H_2 + HOC^+$ $H_2O + C^+ \rightarrow H + HOC^+$ ($n_H \lesssim 2{\times}10^4$ cm^{-3}) $H_2 + CO^+ \rightarrow H + HOC^+$	$HOC^+ + H_2 \rightarrow HCO^+ + H_2$ $HOC^+ + e^- \rightarrow H + CO$ ($n_H \approx 2 \times 10^3$ cm^{-3})
DCO^+	$HCO^+ + D \rightarrow DCO^+ + H$ $CO + CH_4D^+ \rightarrow CH_4 + DCO^+$	$DCO^+ + HCN \rightarrow HDCN^+ + CO$ (T $\gtrsim$ 43 K) $DCO^+ + e^- \rightarrow D + CO$
CO	$HCO^+ + e^- \rightarrow CO + H$ $CO_{ice} \rightarrow CO$ (T $\gtrsim$ 23 K) $CO + He^+ \rightarrow He + O + C^+$	$CO + H_3^+ \rightarrow H_2 + HCO^+$ $CO \rightarrow CO_{ice}$ (T $\gtrsim$ 23K)

In general, we find that two combination of parameters can reproduce the observed values: (1) $t_1 = 0.1$ Myr, $n_H \sim 10^4$ cm^{-3}, $T \sim 32$ K, $\zeta \sim 10^{-16}$ s^{-1} and (2) $n_H \sim 10^4$ cm^{-3}, $T \sim 19$ K, $\zeta \sim 10^{-14}$ s^{-1}. The first combination is only valid for $t_1 = 0.1$ Myr but can explain all the four observed values, while the second one is valid for the two values of t_1 but fails to reproduce the $N(HCO^+)/N(HOC^+)$ unless a higher density ($\sim 10^{5.5}$ cm^{-3}) is adopted. In the second case, either $n_H \sim 10^4$ cm^{-3} or $n_H \sim 10^{5.5}$ cm^{-3} is within the range of density that we derived from the non-LTE analysis of CO, *o*-c-C_3H_2, and CS (see Section 4.1.1). In both cases, the obtained gas temperature satisfies the constraint by the non-LTE analysis of CS lines ($T < 40$ K, see Section 4.1.1). In conclusion, enhanced CR ionization rate ($\sim 10^{-16}$ or $\sim 10^{-14}$ s^{-1}) is required to reproduce the observation according to the simulation.

4.3. *Enhanced CR ionization rate associated with SNR 3C391*

In the previous section, we find an enhanced CR ionization rate associated with SNR 3C391. However, 3C391 is a bright source in X-rays which can penetrate deeper into the MCs compared with UV photons (Wolfire et al. 2022), and induce chemistry similar to CRs (Viti 2017). Chen et al. (2004) found that the X-ray ionization rate of the position towards an 1720 MHz OH maser which is close to 3C391:NML (See Figure 1) is $\zeta_X \sim 2 \times 10^{-15}$ s^{-1}, but their estimation may overestimate the X-ray ionization rate because the equation assumes the X-ray spectrum comprises only photons of 1 keV (Wardle 1999), which have the strongest ionization effect. For a more realistic consideration, we adopt the equations in Appendix A of Maloney et al. (1996) which consider an X-ray spectrum with a photon index of α:

$$\zeta_X \approx 1.83 \times 10^{10} \frac{f_i}{0.4} H_X, \tag{14}$$

where $f_i \approx 0.4$ is the fraction of primary photoelectron energy that goes into ionization, and

$$H_X \approx \frac{3\sigma_0 C_\alpha F_X}{8\tau_1^{\phi+1}} S(\tau_1), \tag{15}$$

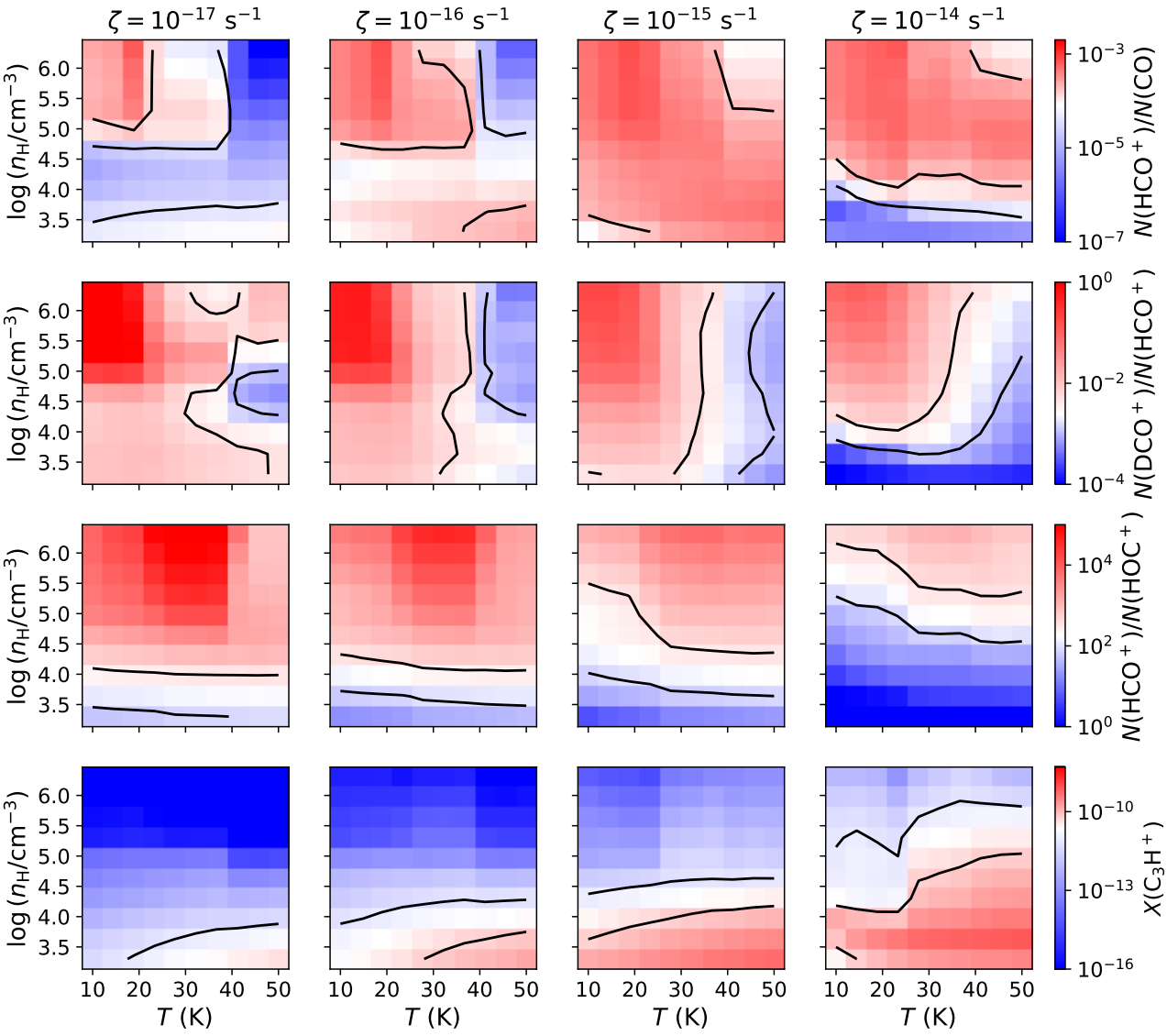

Figure 5. Result of the chemical simulation for $N(\mathrm{HCO^+})/N(\mathrm{CO})$ (upper), $N(\mathrm{DCO^+})/N(\mathrm{HCO^+})$ (middle), and $N(\mathrm{HCO^+})/N(\mathrm{HOC^+})$ (lower) with $t_1 = 0.1$ Myr and C/O = 0.8. The color maps show the abundance ratios given by the simulation. The colorbars are adjusted to have whiter colors with the simulated values closer to the observed ones. Each column shows the results with fixed ζ (CR ionization rate per H_2) from 10^{-17} to 10^{-14} s^{-1}. The black contours show the maximum observed values multiplied by 2 and the minimum observed values divided by 2 as a rough estimate of the uncertainty in observation and calculation. Note that for $N(\mathrm{DCO^+})/N(\mathrm{HCO^+})$ we use the upper limits of $N(\mathrm{DCO^+})$.

where $\sigma_0 = 2.6 \times 10^{-22}$ cm^2, $C_\alpha = (1-\alpha)/(E_{k,\mathrm{max}}^{1-\alpha} - E_{k,\mathrm{min}}^{1-\alpha})$ for $\alpha \neq 1$, $E_{k,\mathrm{min}}$ and $E_{k,\mathrm{max}}$ are the minimum and maximum energies in keV, F_X is the X-ray flux at the target point, $\phi = 3(\alpha-1)/8$, the optical depth at 1 keV from the X-ray source to the target MC is $\tau_1 = 2.6 N_{22}$, and $S(\tau_1) \approx 1$ for $10^{-2} \lesssim \tau_1 \lesssim 10^4$. For 3C391, the X-ray luminosity is 2.3×10^{36} erg s^{-1} in 0.5–10 keV, and the mean distance between 3C391 and 3C391:NML is 7 pc (Chen et al. 2004). The attenuating column density N_H is assumed to be 10^{22} cm^{-2} so that $N_{22} = 1$. We note that ζ_X depends on the X-ray photon index α, but the X-ray spectrum of 3C391 is dominated by a thermal component which cannot be fitted simply with a power law. Assuming $\alpha \approx 3.3$ which is adopted by Zhou et al. (2018) in SNR Cas A, we get $\zeta_\mathrm{X} \sim 3 \times 10^{-20}$ s^{-1} which is significantly lower than the CR ionization rate. Changing the value of α does not affect the basic conclusion that $\zeta_\mathrm{X} < 10^{-19}$ s^{-1}. Although this is just a rough estimation on the order of magnitude of ζ_X, we conclude that the chemistry in 3C391:NML is dominated by CRs instead of X-ray photons.

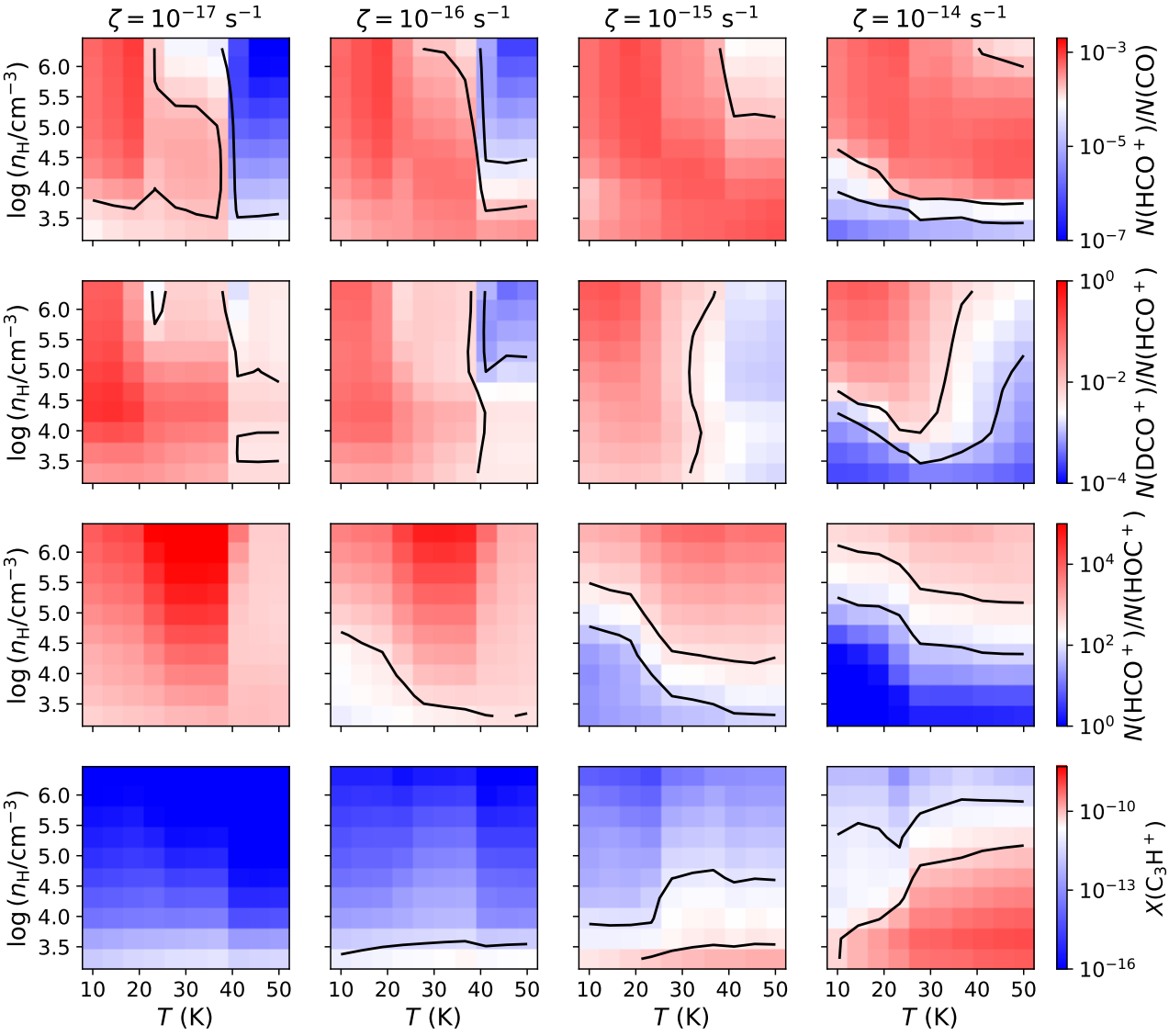

Figure 6. Same as Figure 5 but for $t_1 = 1$ Myr.

The CR ionization rate of $\sim 10^{-16}$ s^{-1} as in the first combination of parameters is higher than the typical values in MCs by an order of magnitude, smaller than the values found in other SNRs ($\sim 10^{-15}$ s^{-1}, e.g. IC443 (Indriolo et al. 2010) and W28 (Vaupré et al. 2014)) by an order of magnitude, but is roughly consistent with the values around SNR W51C found by Yamagishi et al. (2023) using the C^0/CO abundance ratio. We note that this combination of parameters works only when $t_1 = 0.1$ Myr, and that the moderately enhanced temperature, ~ 32 K, requires constraints from further observations, but indeed satisfies the limit (< 40 K) set by the non-LTE analysis of the CS lines.

If $\zeta \sim 10^{-14}$ s^{-1} as in the second combination of parameters is adopted, the observation can also be reproduced by the simulation. Although the observed $N(HCO^+)/N(HOC^+)$ requires higher density ($n_H \sim 10^{5.5}$ cm^{-3}), this value is still roughly consistent with the density we obtained from non-LTE analysis of CS lines. The extremely high value of CR ionization rate is the highest among SNRs, but has been found in the CMZ of our Galaxy (e.g., Oka et al. 2019), the solar-type protostar OMC-2 FIR4 (Ceccarelli et al. 2014; Fontani et al. 2017), and CMZ of other galaxies like NGC 253 (Holdship et al. 2022). The origin of the extremely high CR ionization rate in the CMZ of our Galaxy arises from a combination of energetic activities including SNRs and colliding winds of massive stars (e.g., Yusef-Zadeh et al. 2007), whereas Lattanzi et al. (2023) proposed that the high CR ionization rate in OMC-2 FIR4 is due to the CRs accelerated in the jet shock of the young protostar. However, no star formation activity is found to be asso-

ciated with 3C391:NML (Urquhart et al. 2018). Therefore, it is more likely that the extremely high ζ obtained in 3C391:NML is originated from the SNR. Extrapolating the high energy CR spectrum inferred from the γ-ray observation to low energies, Schuppan et al. (2012) found that SNR 3C391 can induce $\zeta \sim 10^{-14}$ s^{-1} in its surrounding MCs. According to their calculation, a possible reason why 3C391 can induce higher CR ionization rate than other SNRs is that the deduced proton flux of 3C391 at < 1 GeV is higher than those of other SNRs, which means the MCs adjacent to 3C391 is exposed to more ionizing low-energy CR protons. Yet this extrapolation is not exempt from problems, because the CRs leading to ionization have too low energy ($\lesssim 280$ MeV, Padovani et al. 2009) to produce detectable γ-ray emission by available instruments.

Although $\zeta \sim 10^{-14}$ s^{-1} is consistent with the results of chemical simulation, we note that the extremely high CR ionization rate is contradictory to the low temperature (~ 20 K) evidenced by the $I(\mathrm{H^{13}CN})/I(\mathrm{HN^{13}C})$ line ratio and the non-detection of CS 5–4 line (see Section 4.1.1). CR heating is expected to strongly affect the gas temperature when ζ is high. According to Bisbas et al. (2017), the temperature should reach ~ 40 K when $\zeta \sim 10^{-14}$ s^{-1}, while Bayet et al. (2011) gave ~ 80 K at the same ζ. However, we also note that the adopted gas temperature ($T \sim 20$ K) in this study is just a rough estimation: the relation between T and $I(\mathrm{H^{13}CN})/I(\mathrm{HN^{13}C})$ exhibit large scatter (Pazukhin et al. 2022), while the non-LTE analysis of CS may be affected by the unknown beam filling factor. A higher temperature is indeed possible, but further observation is needed. A more robust estimation of the temperature from observation is crucial to the estimation of CR ionization rate in 3C391:NML.

5. CONCLUSION

In this paper, we performed a W band (71.5–90 GHz) line survey with the Yebes 40 m radio telescope towards an unshocked molecular cloud of SNR 3C391, which we call 3C391:NML. Our main conclusions are summarized as follows:

1. We detected 18 molecules in the line survey. The line profile of the $\mathrm{HCO^+}$ $J = 1$–0 line exhibits three components with different linewidths, while most molecular lines only exhibit a narrow component and some exhibit two components.

2. Assuming $T = 20$ K, we estimated the physical parameters of 3C391:NML using the SpectralRadex code with the CO, o-c-$\mathrm{C_3H_2}$ and CS lines. The density is estimated to be $n_{\mathrm{H_2}} \sim 1.4 \times 10^3$ cm^{-3} from the CO lines, and $\sim 2 \times 10^5$ cm^{-3} from the o-c-$\mathrm{C_3H_2}$ and CS lines. The estimated $N_{\mathrm{H_2}}$ of the MC is $\sim 5.8 \times 10^{21}$ cm^{-2}.

3. Using the analytic equations reported by Vaupré et al. (2014), we estimated the CR ionization rate of 3C391:NML is $\gtrsim 2.7 \times 10^{-14}$ s^{-1} with the abundance ratio $N(\mathrm{HCO^+})/N(\mathrm{CO})$ and an upper limit of $N(\mathrm{DCO^+})/N(\mathrm{HCO^+})$. However, we caution on adopting this value because chemical equilibrium, which is a prerequisite of using the equations, is not necessarily reached in the MC considering the 4–19 kyr age of 3C391.

4. We found some unusual abundance and abundance ratios compared with typical values in quiescent dense MCs. They are: $N(\mathrm{HCO^+})/N(\mathrm{HOC^+}) \sim$ 160–180 lower than typical values, $N(\mathrm{HCS^+})/N(\mathrm{CS}) \sim$ 0.14–0.18 higher than typical values, and $X(l\text{-}\mathrm{C_3H^+}) \sim$ 2.9–6.0 $\times 10^{-11}$ higher than typical values by an order of magnitude. These can be attributed to the chemistry induced by CRs. Using the `DNautilus 2.0` chemical model equipped with deuterium chemistry, we present a chemical simulation to explain the observed abundance and abundance ratios. We found that an enhanced CR ionization rate ($\sim 10^{-16}$ or $\sim 10^{-14}$ s^{-1}) is preferred to reproduce the observation. But a more robust estimation of the temperature from observation is crucial to the estimation of CR ionization rate in 3C391:NML.

T.-Y. T. thanks Siyi Feng, Thomas Bisbas, Yichen Sun and Xiao Zhang for helpful discussions. L.M. acknowledges the financial support of DAE and DST-SERB research grants (SRG/2021/002116 and MTR/2021/000864) of the Government of India. Y.C. acknowledges the support from NSFC grants Nos. 12173018 and 12121003. P.Z. acknowledges the support from NSFC grant No. 12273010. M S. G. has carried out the observations and the first inspection of the data quality.

This article is based on observations carried out with the Yebes 40 m telescope (project code: 23A021). The 40 m radio telescope at Yebes Observatory is operated by the Spanish Geographic Institute (IGN; Ministerio de Transportes, Movilidad y Agenda Urbana). This research has also made use of the SIMBAD database, operated at CDS, Strasbourg, France.

Facilities: Yebes, No: 45m, JCMT

Software: astropy (Astropy Collaboration et al. 2018, 2022), Spectral-cube (Ginsburg et al. 2015), GILDAS (Gildas Team, https://www.iram.fr/

IRAMFR/GILDAS/), Montage (http://montage.ipac.caltech.edu/, Matplotlib (https://matplotlib.org))

REFERENCES

Aharonian, F. A. 2013, APh, 43, 71, doi: 10.1016/j.astropartphys.2012.08.007

Albertsson, T., Semenov, D. A., Vasyunin, A. I., Henning, Th., & Herbst, E. 2013, ApJS, 207, 27, doi: 10.1088/0067-0049/207/2/27

Apponi, A. J., & Ziurys, L. M. 1997, ApJ, 481, 800, doi: 10.1086/304080

Astropy Collaboration, Price-Whelan, A. M., Sipőcz, B. M., et al. 2018, ApJ, 156, 123, doi: 10.3847/1538-3881/aabc4f

Astropy Collaboration, Price-Whelan, A. M., Lim, P. L., et al. 2022, ApJ, 935, 167, doi: 10.3847/1538-4357/ac7c74

Bayet, E., Williams, D. A., Hartquist, T. W., & Viti, S. 2011, MNRAS, 414, 1583, doi: 10.1111/j.1365-2966.2011.18500.x

Bisbas, T. G., van Dishoeck, E. F., Papadopoulos, P. P., et al. 2017, ApJ, 839, 90, doi: 10.3847/1538-4357/aa696d

Bohlin, R. C., Savage, B. D., & Drake, J. F. 1978, ApJ, 224, 132, doi: 10.1086/156357

Caselli, P., Walmsley, C. M., Terzieva, R., & Herbst, E. 1998, ApJ, 499, 234, doi: 10.1086/305624

Ceccarelli, C., Dominik, C., López-Sepulcre, A., et al. 2014, ApJ, 790, L1, doi: 10.1088/2041-8205/790/1/L1

Ceccarelli, C., Hily-Blant, P., Montmerle, T., et al. 2011, ApJ, 740, L4, doi: 10.1088/2041-8205/740/1/L4

Cernicharo, J., Agúndez, M., Cabezas, C., et al. 2022, A&A, 657, L16, doi: 10.1051/0004-6361/202142992

Chen, Y., & Slane, P. O. 2001, ApJ, 563, 202, doi: 10.1086/323886

Chen, Y., Su, Y., Slane, P. O., & Wang, Q. D. 2004, ApJ, 616, 885, doi: 10.1086/425152

Cosentino, G., Jiménez-Serra, I., Caselli, P., et al. 2019, ApJ, 881, L42, doi: 10.3847/2041-8213/ab38c5

Ergin, T., Sezer, A., Saha, L., et al. 2014, ApJ, 790, 65, doi: 10.1088/0004-637X/790/1/65

Feng, S., Li, D., Caselli, P., et al. 2020, ApJ, 901, 145, doi: 10.3847/1538-4357/abada3

Ferrand, G., & Safi-Harb, S. 2012, AdSpR, 49, 1313, doi: 10.1016/j.asr.2012.02.004

Fontani, F., Ceccarelli, C., Favre, C., et al. 2017, A&A, 605, A57, doi: 10.1051/0004-6361/201730527

Frail, D. A., Goss, W. M., Reynoso, E. M., et al. 1996, ApJ, 111, 1651, doi: 10.1086/117904

Frerking, M. A., Langer, W. D., & Wilson, R. W. 1982, ApJ, 262, 590, doi: 10.1086/160451

Fuente, A., García-Burillo, S., Usero, A., et al. 2008, A&A, 492, 675, doi: 10.1051/0004-6361:200810571

Fuente, A., Cernicharo, J., Roueff, E., et al. 2016, A&A, 593, A94, doi: 10.1051/0004-6361/201628285

Gerin, M., Liszt, H., Neufeld, D., et al. 2019, A&A, 622, A26, doi: 10.1051/0004-6361/201833661

Ginsburg, A., Robitaille, T., Beaumont, C., et al. 2015, in ASP Conference Series, Vol. 499 (San Francisco: Astronomical Society of the Pacific), 363–364

Glassgold, A. E., & Langer, W. D. 1974, ApJ, 193, 73, doi: 10.1086/153130

Goicoechea, J. R., Pety, J., Gerin, M., Hily-Blant, P., & Le Bourlot, J. 2009, A&A, 498, 771, doi: 10.1051/0004-6361/200811496

Goicoechea, J. R., Cuadrado, S., Pety, J., et al. 2017, A&A, 601, L9, doi: 10.1051/0004-6361/201730716

Guzmán, V. V., Pety, J., Goicoechea, J. R., et al. 2015, ApJ, 800, L33, doi: 10.1088/2041-8205/800/2/L33

Harada, N., Martín, S., Mangum, J. G., et al. 2021, ApJ, 923, 24, doi: 10.3847/1538-4357/ac26b8

Hasegawa, T. I., & Herbst, E. 1993, MNRAS, 261, 83, doi: 10.1093/mnras/261.1.83

Holdship, J., Mangum, J. G., Viti, S., et al. 2022, ApJ, 931, 89, doi: 10.3847/1538-4357/ac6753

Indriolo, N., Blake, G. A., Goto, M., et al. 2010, ApJ, 724, 1357, doi: 10.1088/0004-637X/724/2/1357

Jiang, B., Chen, Y., Wang, J., et al. 2010, ApJ, 712, 1147, doi: 10.1088/0004-637X/712/2/1147

Lattanzi, V., Alves, F. O., Padovani, M., et al. 2023, A&A, 671, A35, doi: 10.1051/0004-6361/202142736

Leahy, D. A., & Ranasinghe, S. 2018, ApJ, 866, 9, doi: 10.3847/1538-4357/aade48

Linsky, J. L., Draine, B. T., Moos, H. W., et al. 2006, ApJ, 647, 1106, doi: 10.1086/505556

Liszt, H., Lucas, R., & Black, J. H. 2004, A&A, 428, 117, doi: 10.1051/0004-6361:20041649

Liu, X. C., Wu, Y., Zhang, C., et al. 2021, ApJ, 912, 148, doi: 10.3847/1538-4357/abee73

Loison, J.-C., Wakelam, V., Hickson, K. M., Bergeat, A., & Mereau, R. 2014, MNRAS, 437, 930, doi: 10.1093/mnras/stt1956

Majumdar, L., Gratier, P., Ruaud, M., et al. 2017, MNRAS, 466, 4470, doi: 10.1093/mnras/stw3360

Maloney, P. R., Hollenbach, D. J., & Tielens, A. G. G. M. 1996, ApJ, 466, 561, doi: 10.1086/177532

Mangum, J. G., & Shirley, Y. L. 2015, PASA, 127, 266, doi: 10.1086/680323

Milam, S. N., Savage, C., Brewster, M. A., Ziurys, L. M., & Wyckoff, S. 2005, ApJ, 634, 1126, doi: 10.1086/497123

Nesterenok, A. V. 2022, MNRAS, 509, 4555, doi: 10.1093/mnras/stab3303

Oka, T., Geballe, T. R., Goto, M., et al. 2019, ApJ, 883, 54, doi: 10.3847/1538-4357/ab3647

Padovani, M., Galli, D., & Glassgold, A. E. 2009, A&A, 501, 619, doi: 10.1051/0004-6361/200911794

Park, G., Currie, M. J., Thomas, H. S., et al. 2023, ApJS, 264, 16, doi: 10.3847/1538-4365/ac9b59

Paulive, A., Carder, J. T., & Herbst, E. 2022, MNRAS, 516, 4097, doi: 10.1093/mnras/stac2507

Paulive, A., Shingledecker, C. N., & Herbst, E. 2021, MNRAS, 500, 3414, doi: 10.1093/mnras/staa3458

Pazukhin, A. G., Zinchenko, I. I., Trofimova, E. A., & Henkel, C. 2022, ARep, 66, 1302, doi: 10.1134/S1063772922110154

Pety, J., Gratier, P., Guzmán, V., et al. 2012, A&A, 548, A68, doi: 10.1051/0004-6361/201220062

Podio, L., Lefloch, B., Ceccarelli, C., Codella, C., & Bachiller, R. 2014, A&A, 565, A64, doi: 10.1051/0004-6361/201322928

Pratap, P., Dickens, J. E., Snell, R. L., et al. 1997, ApJ, 486, 862, doi: 10.1086/304553

Ranasinghe, S., & Leahy, D. 2022, ApJ, 940, 63, doi: 10.3847/1538-4357/ac940a

Reach, W. T., & Rho, J. 1996, A&A, 315, L277

—. 1998, ApJ, 507, L93, doi: 10.1086/311672

—. 1999, ApJ, 511, 836, doi: 10.1086/306703

—. 2000, ApJ, 544, 843, doi: 10.1086/317252

Reboussin, L., Wakelam, V., Guilloteau, S., & Hersant, F. 2014, MNRAS, 440, 3557, doi: 10.1093/mnras/stu462

Reynolds, S. P., & Moffett, D. A. 1993, AJ, 105, 2226, doi: 10.1086/116600

Rho, J. H., & Petre, R. 1996, ApJ, 467, 698, doi: 10.1086/177645

Rodríguez-Baras, M., Fuente, A., Riviére-Marichalar, P., et al. 2021, A&A, 648, A120, doi: 10.1051/0004-6361/202040112

Ruaud, M., Wakelam, V., & Hersant, F. 2016, MNRAS, 459, 3756, doi: 10.1093/mnras/stw887

Sato, T., Koyama, K., Takahashi, T., Odaka, H., & Nakashima, S. 2014, PASJ, 66, 124, doi: 10.1093/pasj/psu120

Schuppan, F., Becker, J. K., Black, J. H., & Casanova, S. 2012, A&A, 541, A126, doi: 10.1051/0004-6361/201218849

Shingledecker, C. N., Tennis, J., Le Gal, R., & Herbst, E. 2018, ApJ, 861, 20, doi: 10.3847/1538-4357/aac5ee

Spitzer, L. 1978, Physical Processes in the Interstellar Medium, doi: 10.1002/9783527617722

Sternberg, A., Dalgarno, A., & Lepp, S. 1987, ApJ, 320, 676, doi: 10.1086/165585

Taniguchi, K., Rayalacheruvu, P., Yonetsu, T., et al. 2024, ApJ, 963, 12, doi: 10.3847/1538-4357/ad1e5a

Tu, T.-Y., Chen, Y., Zhou, P., & Safi-Harb, S. 2024, Shock and Cosmic Ray Chemistry Associated with the Supernova Remnant W28, doi: 10.48550/arXiv.2403.13305

Umemoto, T., Minamidani, T., Kuno, N., et al. 2017, PASJ, 69, 78, doi: 10.1093/pasj/psx061

Urquhart, J. S., König, C., Giannetti, A., et al. 2018, MNRAS, 473, 1059, doi: 10.1093/mnras/stx2258

van der Tak, F. F. S., Black, J. H., Schöier, F. L., Jansen, D. J., & van Dishoeck, E. F. 2007, A&A, 468, 627, doi: 10.1051/0004-6361:20066820

van der Tak, F. F. S., Lique, F., Faure, A., Black, J. H., & van Dishoeck, E. F. 2020, Atoms, 8, 15, doi: 10.3390/atoms8020015

Vaupré, S., Hily-Blant, P., Ceccarelli, C., et al. 2014, A&A, 568, A50, doi: 10.1051/0004-6361/201424036

Vidal, T. H. G., Loison, J.-C., Jaziri, A. Y., et al. 2017, MNRAS, 469, 435, doi: 10.1093/mnras/stx828

Viti, S. 2017, A&A, 607, A118, doi: 10.1051/0004-6361/201628877

Wakelam, V., Dartois, E., Chabot, M., et al. 2021, A&A, 652, A63, doi: 10.1051/0004-6361/202039855

Wardle, M. 1999, ApJ, 525, L101, doi: 10.1086/312351

Wenger, M., Ochsenbein, F., Egret, D., et al. 2000, A&AS, 143, 9, doi: 10.1051/aas:2000332

Wolfire, M. G., Vallini, L., & Chevance, M. 2022, ARA&A, 60, 247, doi: 10.1146/annurev-astro-052920-010254

Yamagishi, M., Furuya, K., Sano, H., et al. 2023, PASJ, 75, 883, doi: 10.1093/pasj/psad046

Yan, Y. T., Henkel, C., Kobayashi, C., et al. 2023, A&A, 670, A98, doi: 10.1051/0004-6361/202244584

Yusef-Zadeh, F., Muno, M., Wardle, M., & Lis, D. C. 2007, ApJ, 656, 847, doi: 10.1086/510663

Zhou, P., Li, J.-T., Zhang, Z.-Y., et al. 2018, ApJ, 865, 6, doi: 10.3847/1538-4357/aad960

Zhou, P., Zhang, G.-Y., Zhou, X., et al. 2022, ApJ, 931, 144, doi: 10.3847/1538-4357/ac63b5